Electronic Supplementary Material (ESI) for Inorganic Chemistry Frontiers.


# Designing Ce single-atom-sites coupled with $CeO_2$ nanoparticles for oxygen reduction enhancement

Jianping Liu[a,b], Guijun Li[b,c], Chuanlan Xu[d], Hongdian Chen[a,b], Rong Jin[b,e], Lingtao Sun[b,e], Chenyang Shu[a,b], Haifeng Chen [b], Chaozhong Guo[a,b,e*], Honglin Li[f*], Yujun Si[c*]

[a] School of Chemistry and Chemical Engineering, Chongqing University of Technology, Chongqing 400054, China.

[b] Chongqing Key Laboratory of Materials Surface & Interface Science, Chongqing University of Arts and Sciences, Chongqing 402160, China.

[c] College of Chemistry and Environmental Engineering, Sichuan University of Science and Engineering, Zigong 643000, China.

[d] College of Chemistry and Chemical Engineering, Chongqing University, Chongqing 401331, China.

[e] Institute of Chemical and Gas and Oil Technologies, T.F. Gorbachev Kuzbass State Technical University, Kemerovo 650000, Russia.

[f] School of Physics and Electronic Engineering, Chongqing Normal University, Chongqing 401331, China.

***Corresponding authors.**

*Email addresses:* guochaozhong1987@163.com (C. Guo); syj08448@163.com (Y. Si); 172093818@163.com (H. Li)

**Electrochemical tests**

The catalyst ink was prepared by weighing 1 mg $CeO_2$/ SACe-N-C catalyst in 160 μL water, 20 μL isopropanol and 20 μL Nafion. The catalyst ink was dispersed by ultrasound for 15 min, and 15 μL uniformly dispersed catalytic ink was dripped onto the surface of the disc electrode with a load of 0.384 mg $cm^{-2}$ by pipetting gun, and dried at room temperature. The electrochemical test was performed on CHI 760E electrochemical workstation with 0.1 M KOH solution as electrolyte, oxygen flow rate of 100, graphite rod as counter electrode and controlled Hg/HgO as reference electrode. Cyclic voltammetry (CV) tests were performed under $N_2$ or $O_2$ saturation conditions at 50 mV/s in 0.1 M KOH solution, and linear scan voltammetry (LSV) was performed at 1600 rpm from 0 V to 1.1 V at 10 mV/s. The $H_2O_2$ % and transferred electron number (n) of the ORR were calculated via using the Eqs (1) and (2):

$$H_2H_2(\%) = 200 \times \frac{I_R/N}{(I_R/N) + I_D} \quad (1)$$

$$n = 4 \times \frac{I_D}{(I_R/N) + I_D} \quad (2)$$

In which $I_R$ and $I_D$ are ring and disk current; the current collection efficiency of the n is 0.38.

The K–L equation:

$$\frac{1}{J} = \frac{1}{J_k} + \frac{1}{J_d} = \frac{1}{J_k} + \frac{1}{Bw^{1/2}} \quad (3)$$

$$B = 0.2nFC_0 D_0^{2/3} V^{-1/6} \quad (4)$$

In which J, $J_k$ and $J_d$ are the measured current density, the kinetic current density and the diffusion-limiting current density, respectively; ω is the angular velocity; n and F are the electron transfer number and the Faraday constant (96485 C $mol^{-1}$); $C_0$ and $D_0$ are the bulk concentration of $O_2$ ($1.2 \times 10^{-6}$ mol $cm^{-3}$) and the diffusion coefficient of

$O_2$ ($1.9 \times 10^{-5}$ $cm^2$ $s^{-1}$); V is the kinematic viscosity of the electrolyte (0.01 $cm^2$ $s^{-1}$).

The $J_k$ were calculated as follow:

$$J_k = \frac{J_d * J}{J_d - J} \quad (5)$$

Tafel slopes were calculated:

$$\eta = a + blog(\frac{j}{j_0}) \quad (6)$$

in which η, b, j, and $j_0$ are the overpotential, the Tafel slope, the current density and the exchange current density, respectively.

**Zn-air battery test**

2 mg of $CeO_2$/SACe-N-C catalyst was uniformly dispersed in 195 μL ethanol and 5 μL Nafion (5 wt.%), and the catalyst ink was uniformly coated on carbon paper (2x2 cm) as the air cathode, nickel foam was used as the fluid collector, and zinc plate was used as the metal anode to assemble zinc-air battery. The battery performance was tested in 6 M KOH solution. $CeO_2$/SACe-N-C and Pt/C were loaded with 0.5 mg $cm^{-2}$.

**Theoretical calculation**

In this work, the initial models of different structures were built using VESTA.[1-6] For the exchange and correlation energies, the generalized gradient approximation (GGA) in the form of Perdew-Burke-Ernzerhof (PBE) functional is adopted.[7] Considering the reality that the vdW interaction has an unneglected effect on the final stability of the heterostructures, the standard PBE function cannot handle this weak interaction well, so we adopted the DFT-D2 method by Grimme to describe the weak vdW interaction in all calculations,[8] in which all the force field parameters are obtained based on the PBE function. The total energy ($E_{total}$) is expressed as: $E_{total} = E_{KS}\text{-}DFT + E_{vdW}$, where $E_{KS}\text{-}DFT$ and $E_{vdW}$ are Kohn-Sham DFT energy and dispersion correction respectively.[9, 10] The first Brillouin-zone sampling of 1×1×1 and 5×4×1 k-points generated by

Monkhorst-Pack scheme are used for geometric optimization and energy calculations, respectively. The vacuum layer is set to 20 Å along the Z direction to avoid the interactions induced by the periodic effects. To find a balance between accuracy and efficiency, a 450 eV cut-off energy has been adopted in all calculations. The pristine and heterojunction structures were optimized until the forces on each atom are less than $10^{-4}$ eV and the Hellmann-Feynman force on each atom is 0.01 eV $Å^{-1}$, which was sufficient enough to reach convergence for the whole calculations. The charge density different is obtained by: $\Delta\rho = \rho^{AB} - \rho^{A} - \rho^{B}$.

The free energies of reactants and each intermediate state at an applied electrode potential U were calculated as follows: $\Delta G = \Delta E + \Delta ZPE - T\Delta S - neU$, where n is the electron number of such state and $\Delta E$ represents the change in enthalpy which is considered from the DFT total energy value, $\Delta ZPE$ represents the change in zero-point energy and $\Delta S$ represents the change in entropy. Since it is difficult to obtain the exact free energy of OOH, O, and OH radicals in the electrolyte solution, the adsorption free energy $\Delta G_{OOH*}$, $\Delta G_{O*}$, and $\Delta G_{OH*}$ are used in the calculations. The equilibrium potential $U_0$ for ORR at pH = 13 was determined to be 0.455 V *vs.* NHE where the reactant and product are at the same energy level. The free energy of $H_2O$(l) was derived as $G_{H2O(l)} = G_{H2O(g)} + RT*\ln(p/p_0)$ since only $G_{H2O(g)}$ can be directly obtained by DFT calculations. The free energy of $O_2$(g) was derived as $G_{O2(g)} = 2G_{H2O(l)} - 2G_{H2} - 1.82$ eV.[11] The free energy of $OH^-$ was derived as $G_{OH^-} = G_{H2O(l)} - G_{H+}$, where $G_{H+} = 1/2G_{H2} - k_BT\ln10 * pH$. The overall reaction scheme of ORR in alkaline environment is: $O_2 + 2H_2O + 4e^- \rightarrow 4OH^-$,[12] and the following associative mechanism is considered in our calculations:

$$O_2(g) + * + H_2O + e^- \leftrightarrows *OOH + OH^- \quad (1)$$

$$*OOH + e^- \leftrightarrows *O + OH^- \quad (2)$$

$$*O + H_2O + e^- \leftrightarrows *OH + OH^- \quad (3)$$

$$*OH + e^- \leftrightarrows * + OH^- \quad (4)$$

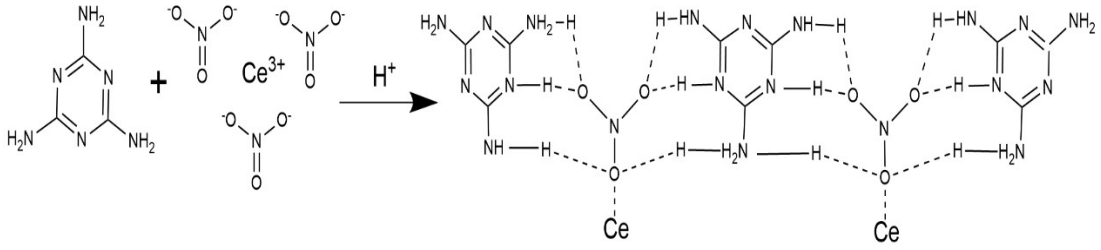


**Figure S1**. Schematic diagram of protonated melamine self-assembly.

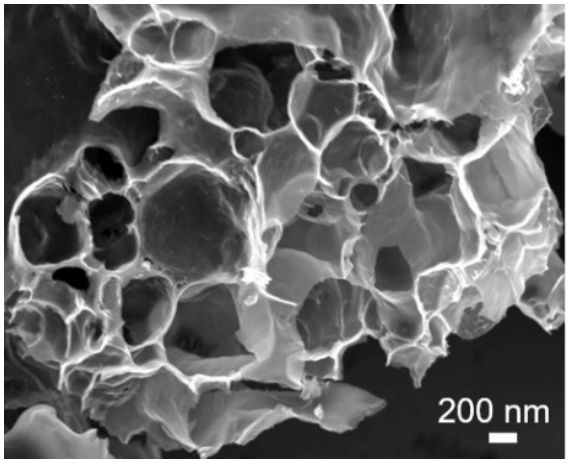


**Figure S2**. SEM of $CeO_2$/SACe-N-C catalyst.

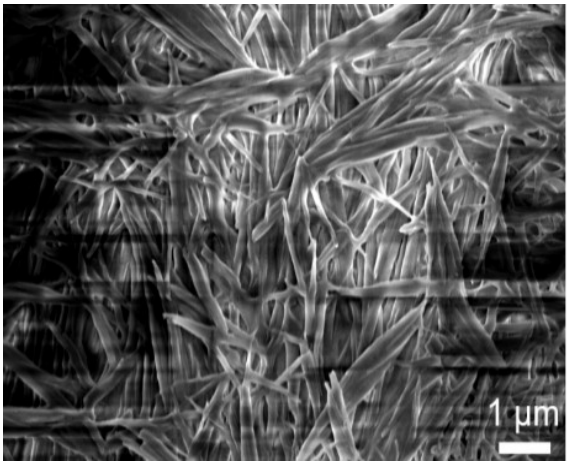


**Figure S3**. SEM of $CeO_2$/SACe-N-C precursor.


**Figure S4**. SEM of N-C precursor.

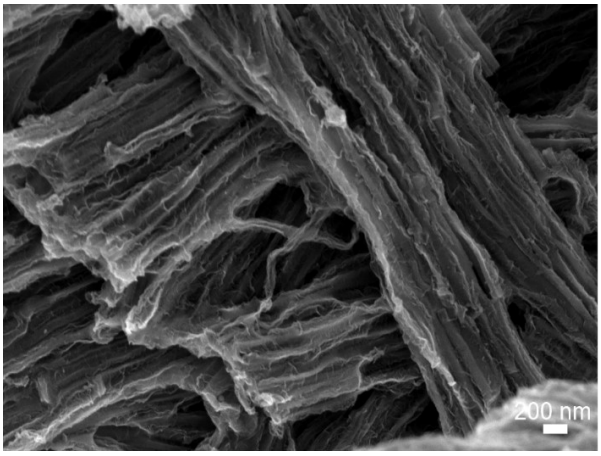


**Figure S5**. SEM of N-C catalyst.

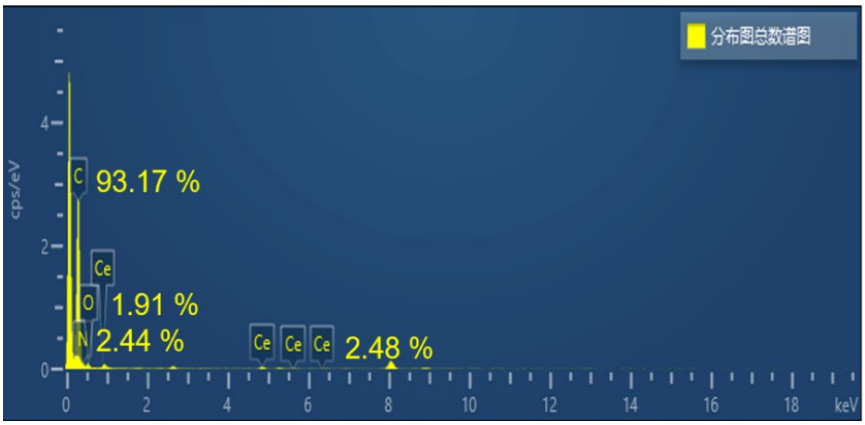


**Figure S6**. EDS spectrum of $CeO_2$/SACe-N-C.

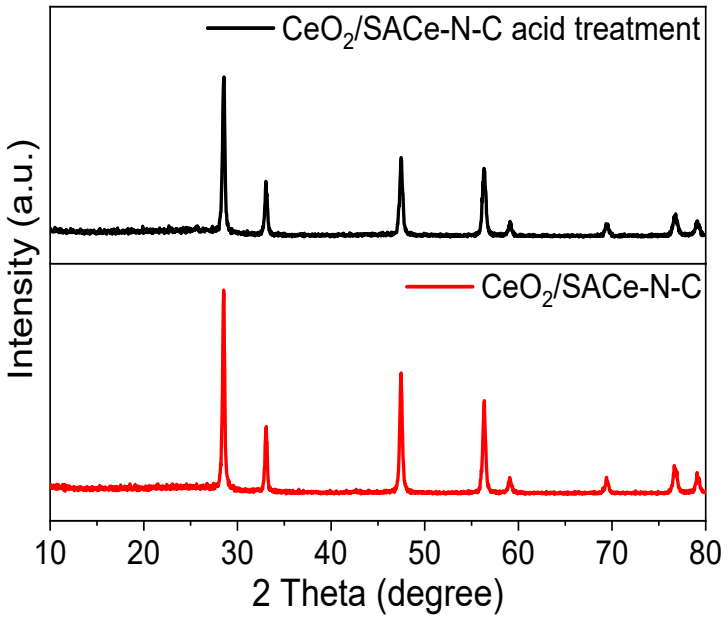


**Figure S7**. XRD spectrum of $CeO_2$/SACe-N-C and after $CeO_2$/SACe-N-C acid treatment.

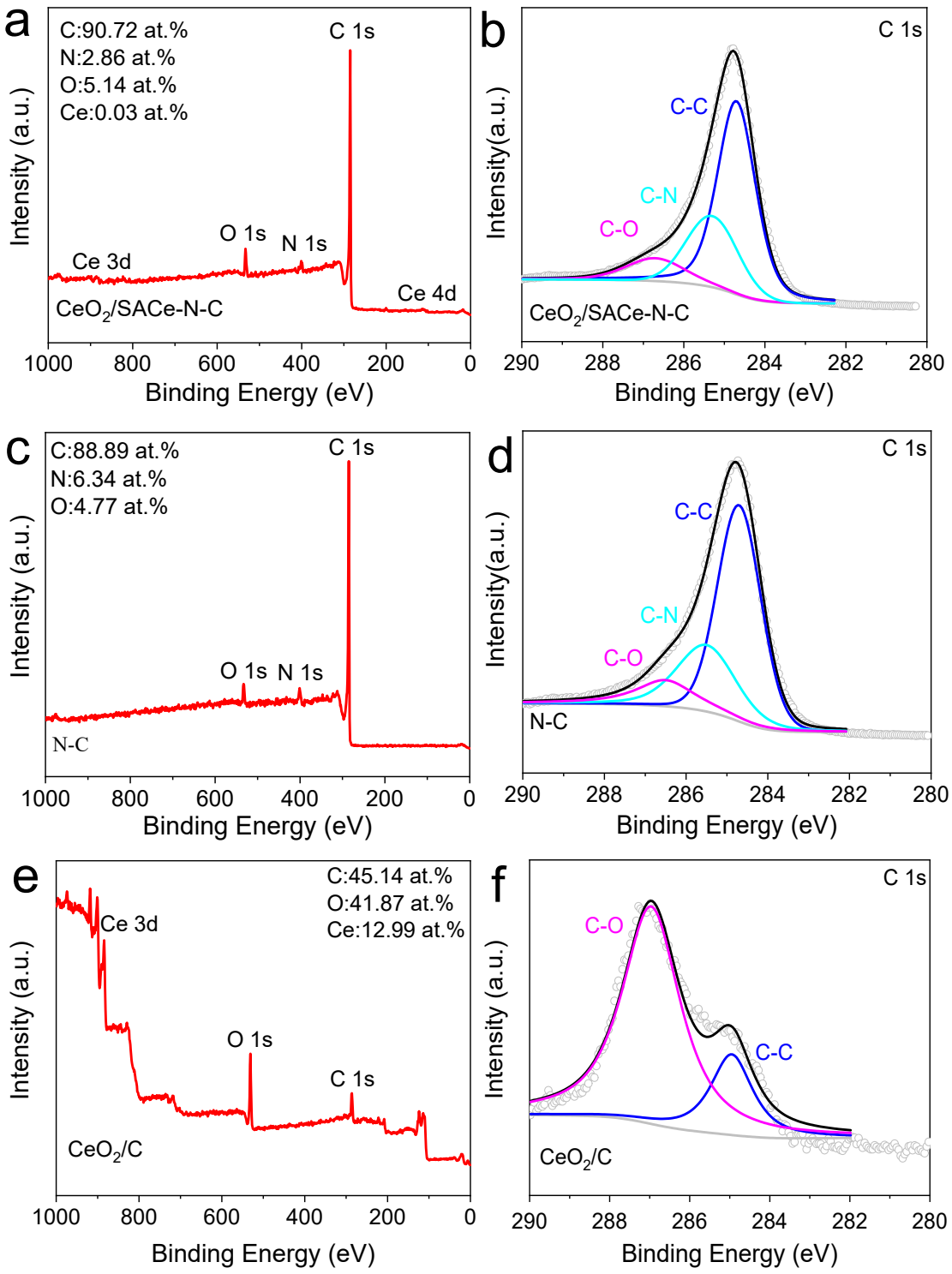


**Figures S8**. a, c, e) XPS survey of the corresponding catalyst; b, d, f) High resolution XPS spectra of C 1s for catalyst.

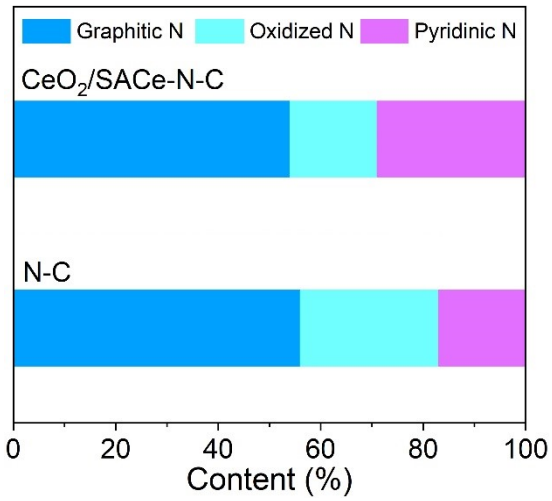


**Figures S9.** Proportion of different N species in $CeO_2$/SACe-N-C and N-C.

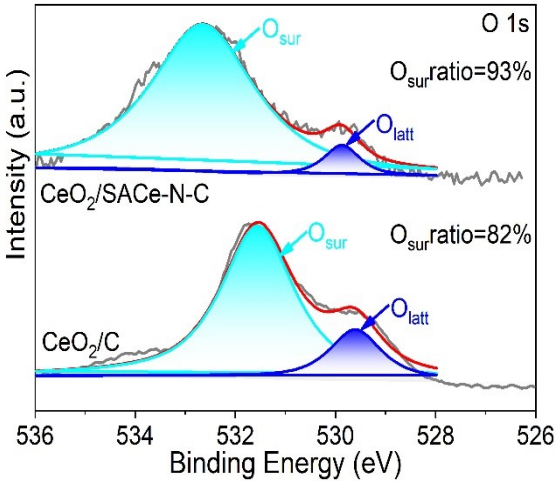


**Figures S10.** High resolution XPS spectra of O 1s for $CeO_2$/SACe-N-C and $CeO_2$/C catalyst.

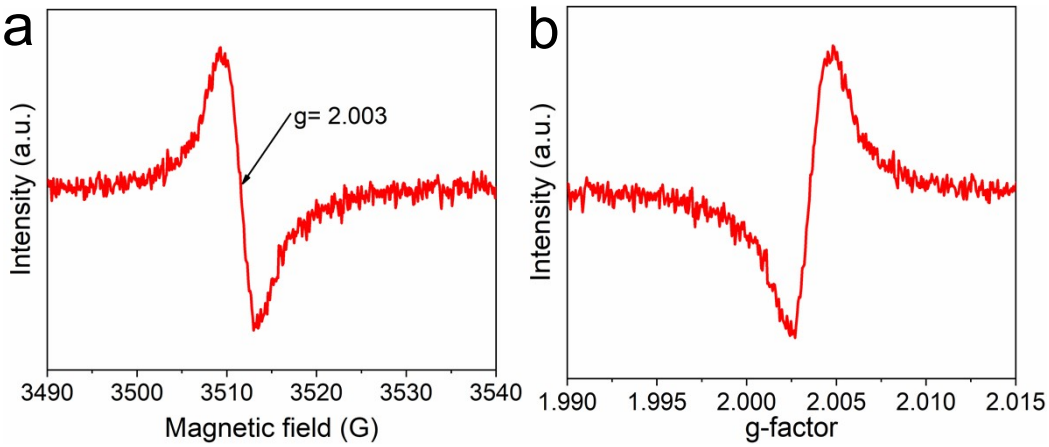


**Figures S11. (a, b)** EPR spectra of $CeO_2$/SACe-N-C catalyst.

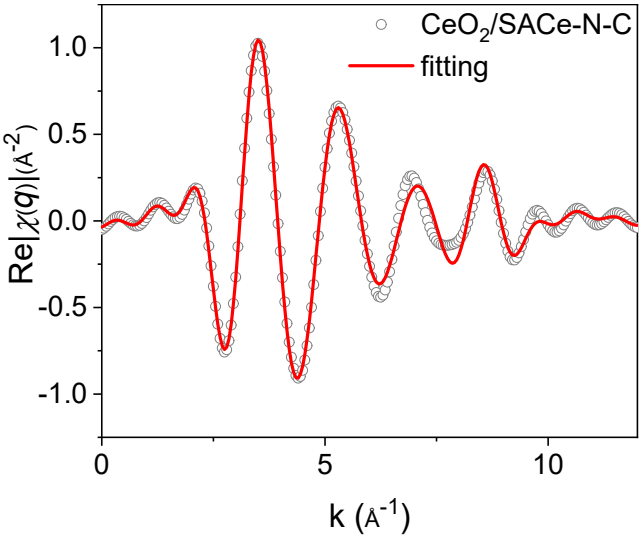


**Figure S12**. FT-EXAFS fitting curves of $CeO_2$/SACe-N-C catalyst at K-space.

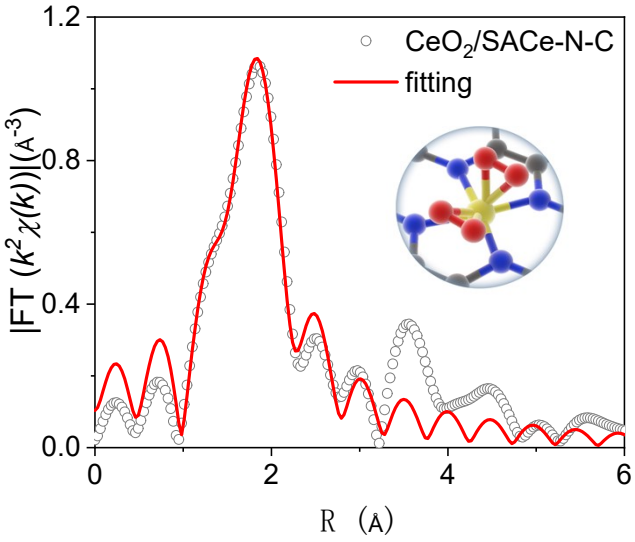


**Figure S13**. FT-EXAFS fitting curves of $CeO_2$/SACe-N-C catalyst at R-space; inset is coordination structure of Ce-$N_4$/$O_4$.

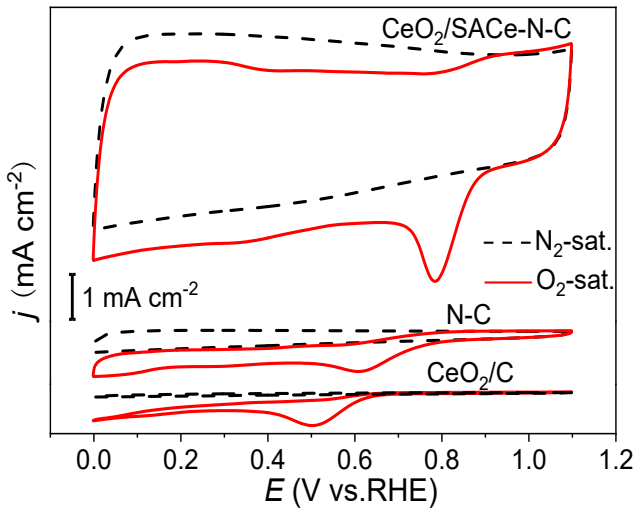


**Figures S14**. CV curves of $CeO_2$/C, N-C and $CeO_2$/SACe-N-C catalysts tested in 0.1 M KOH solution saturated with $O_2$ or $N_2$.

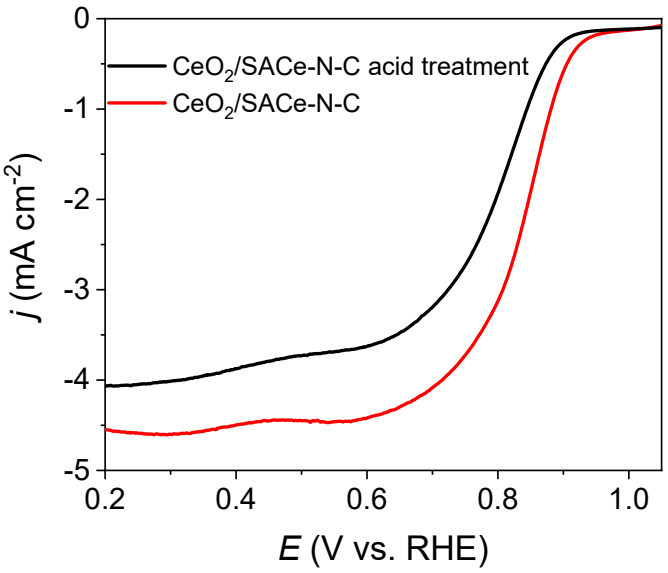


**Figures S15**. LSV curves of $CeO_2$/SACe-N-C catalysts and after $CeO_2$/SACe-N-C acid treatment tested in 0.1 M KOH solution saturated with $O_2$.

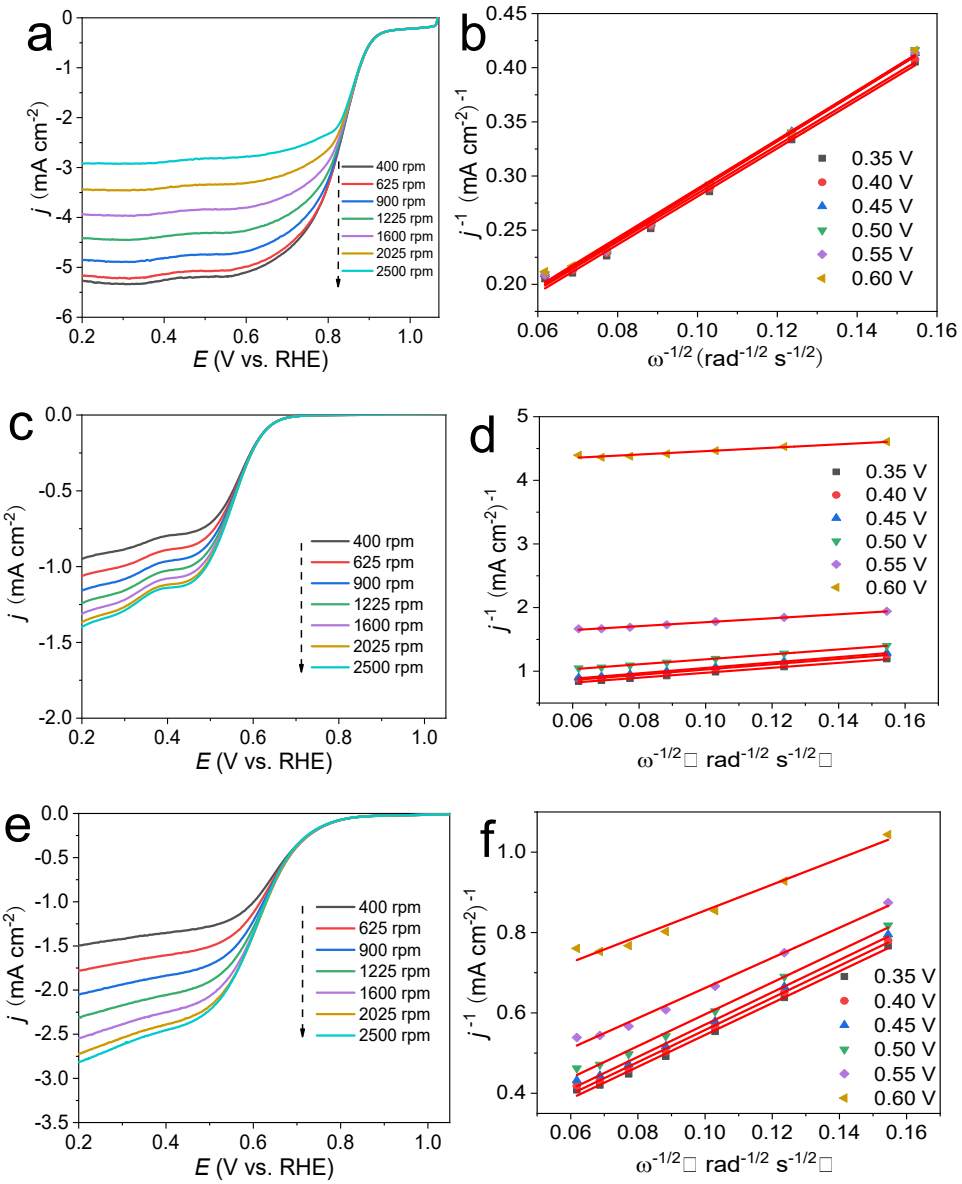


**Figures S16**. a, c, e) LSV curves of $CeO_2$/SACe-N-C, $CeO_2$/C and N-C at different speeds; b, d, f) the corresponding K-L plots.

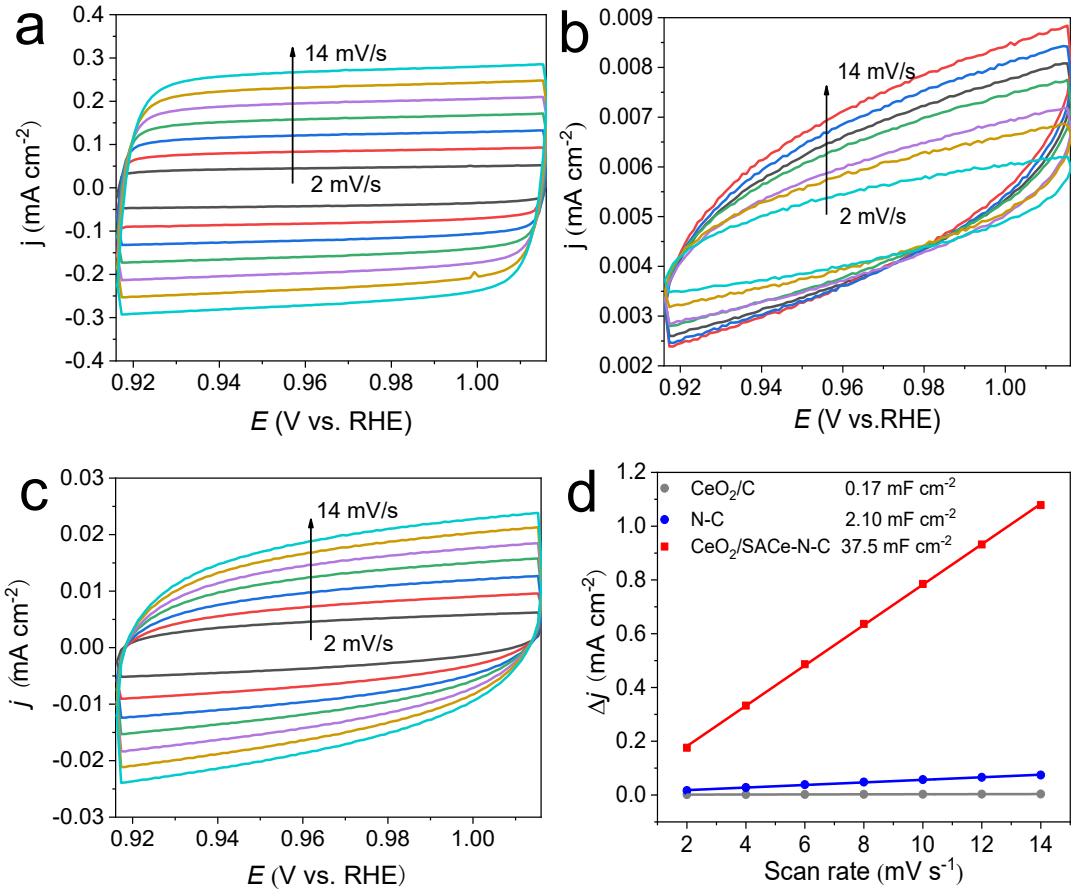


**Figures S17**. a-c) CV curves of $CeO_2$/SACe-N-C, $CeO_2$/C and N-C at different scanning speeds in the non-Faradaic potential range; d) Double-layer capacitance of corresponding catalysts.

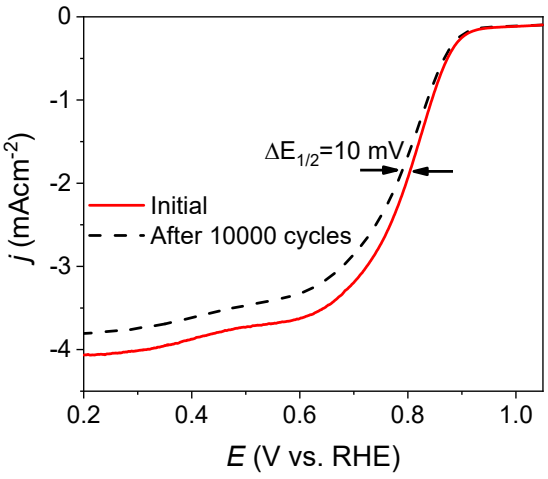


**Figure S18**. LSV curves of after $CeO_2$/SACe-N-C acid treatment catalyst before and after 10000 cycles at 1600 rpm.

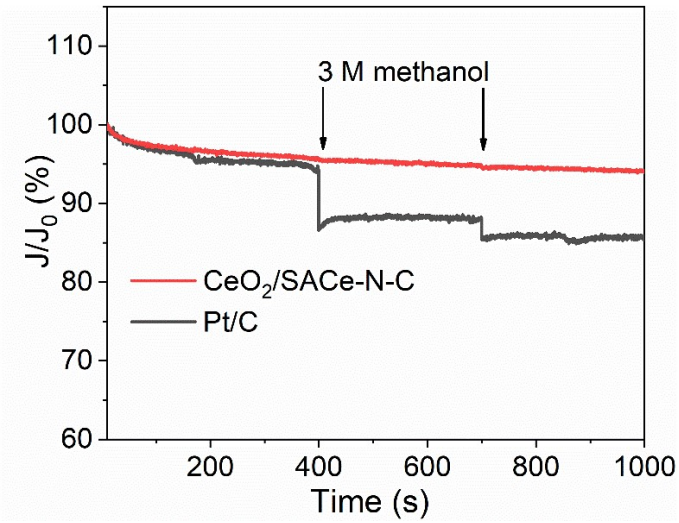


**Figure S19**. I-t curves of $CeO_2$/SACe-N-C and commercial Pt/C catalysts after two additions of 3 M methanol.

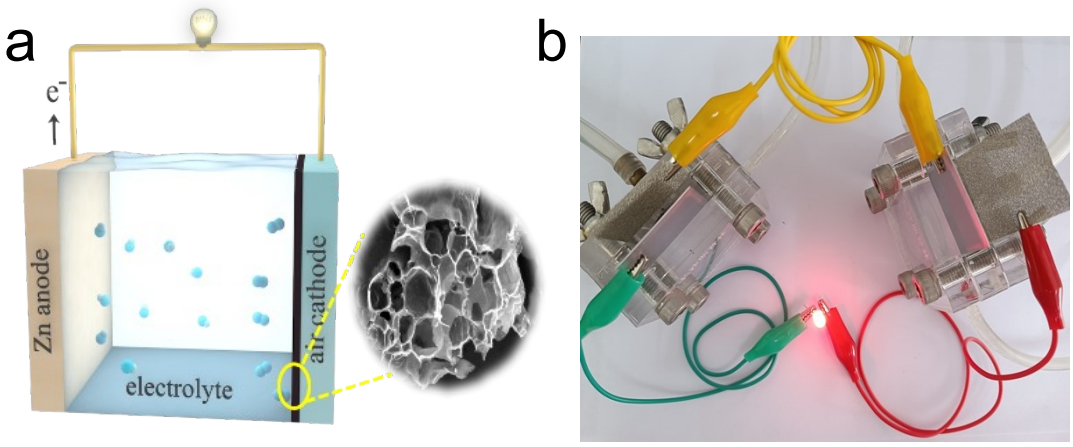


**Figure S20**. a-b) Schematic diagram and real product photo of Zn-air batteries.

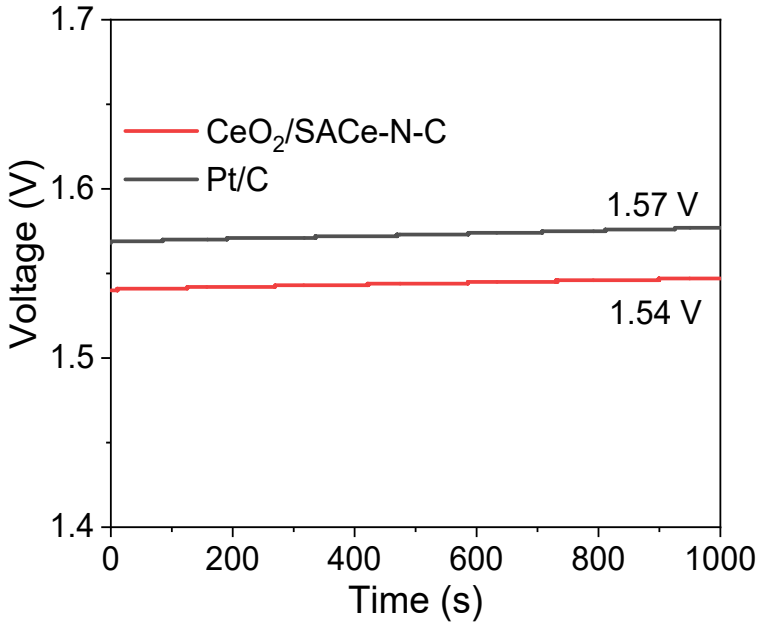


**Figure S21**. Open-circuit voltage curves of Zn-air batteries based on $CeO_2$/SACe-N-C and Pt/C catalyst.

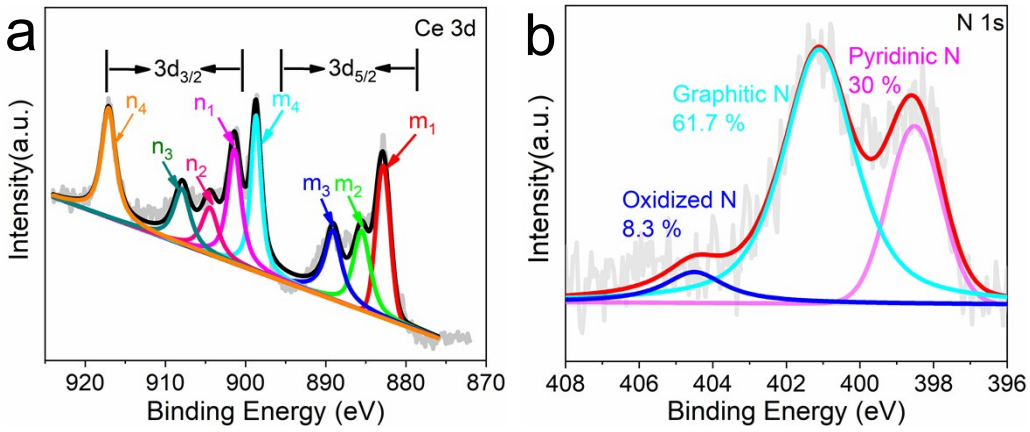


**Figures S22**. a-b) High resolution XPS spectra of Ce 3d and N 1s for $CeO_2$/SACe-N-C catalyst after doing continuous charge-discharge tests of 300 cycles.

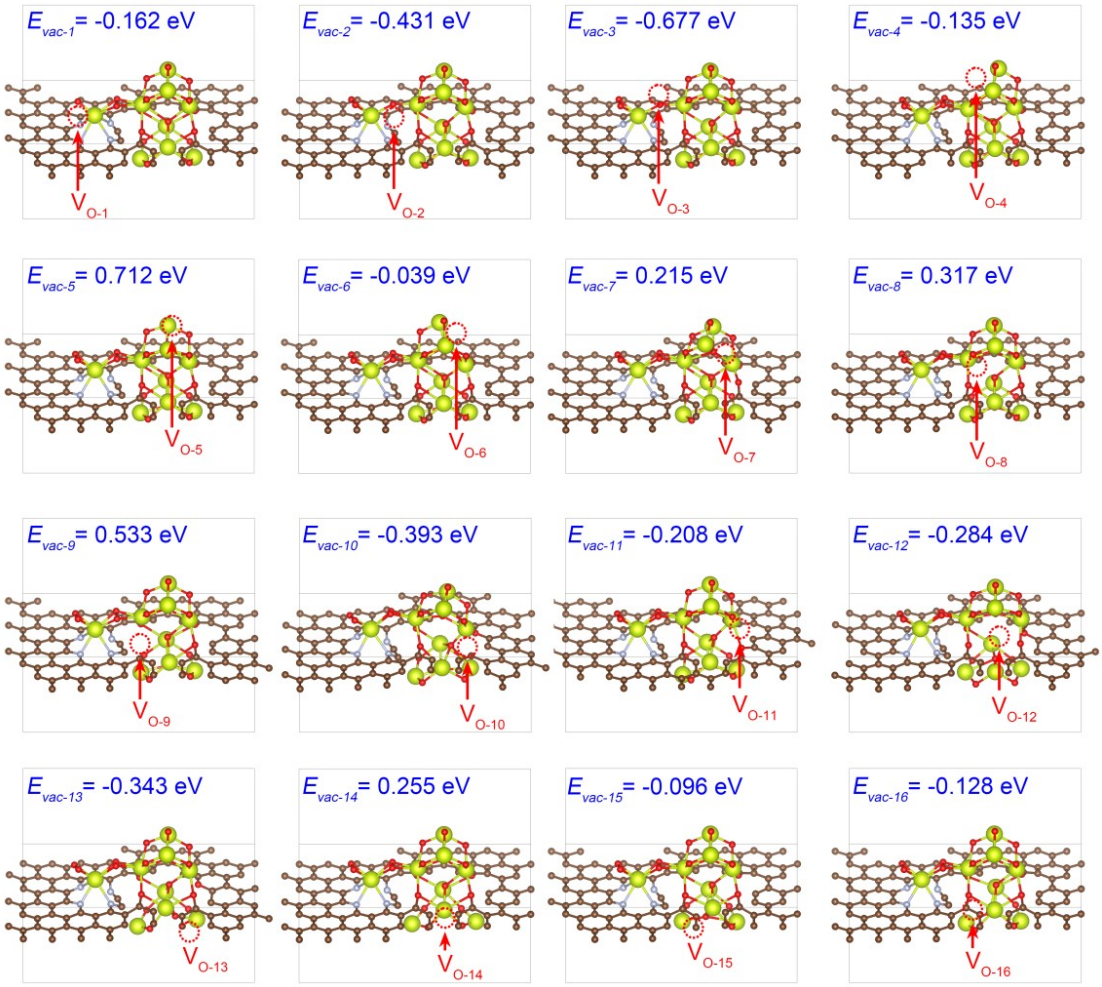


**Figure S23**. The geometric configuration of 16 different oxygen defect configurations in Ce-$N_4O_4$-$CeO_2$. The red circle denotes the vacancy position of oxygen atom.

**Table S1**.EDS element distribution spectrum of $CeO_2$/SACe-N-C catalyst.

| Element distribution spectrum | element | C | N | O | Ce | total |
|---|---|---|---|---|---|---|
| | Wt% | 93.17 | 2.44 | 1.91 | 2.48 | 100.00 |

**Table S2**. BET surface area and pore distribution of $CeO_2$/C, N-C and $CeO_2$/SACe-N-C catalyst.

| | $CeO_2$/C | N-C | $CeO_2$/SACe-N-C |
|---|---|---|---|
| Vmicro ($cm^3/g$) | 0.0005 | 0.02 | 0.15 |
| Smicro ($m^2/g$) | 1.20 | 43.57 | 298.25 |
| Vtotal ($cm^3/g$) | 0.07 | 0.27 | 0.45 |
| $S_{BET}$ ($m^2/g$) | 19.73 | 125.00 | 592.65 |
| Vmicro / Vtotal (%) | 0.82 | 8.24 | 32.39 |
| Smicro / $S_{BET}$ (%) | 6.07 | 34.86 | 50.33 |

**Table S3**. Proportion of $Ce^{3+}$ and $Ce^{4+}$ for $CeO_2$/C and $CeO_2$/SACe-N-C.

| | $Ce^{3+}$ | $Ce^{4+}$ |
|---|---|---|
| $CeO_2$/SACe-N-C | 32.6% | 67.4% |
| $CeO_2$/ C | 17.5% | 82.5% |

**Table S4**. EXAFS fitting results for $CeO_2$, $CeCl_3$ and $CeO_2$/SACe-N-C at the Ce $L_3$-edge.

| Sample | Path | C.N. | R (Å) | $\sigma^2\times10^3$ (Å$^2$) | ΔE (eV) | R factor |
|---|---|---|---|---|---|---|
| $CeO_2$ | Ce-O | 8* | 2.37±0.02 | 9.8±4.6 | 4.0±1.9 | 0.018 |
| $CeCl_3$ | Ce-Cl | 6.1±3.2 | 2.91±0.05 | 16.1±9.4 | 2.5±3.8 | 0.013 |
| $CeO_2$/SACe-N-C | Ce-N<br>Ce-O | 3.9 ± 0.6 3.9 ± 0.8 | 2.38±0.01<br>2.42±0.01 | 0.0117±0.003 3<br>0.0117±0.003 3 | 7.8 ± 1.2 | 0.0054 |

C.N.: coordination numbers; R: bond distance; $\sigma^2$: Debye-Waller factors; ΔE: the inner potential correction. R factor: goodness of fit. * fitting with fixed parameter.

**Table S5**. The properlties of $CeO_2$/SACe-N-C were compared with other catalysts.

| Catalyst | Catalyst loading (mg cm$^{-2}$) | $E_{1/2}$(V) | $E_{onset}$(V) | References |
|---|---|---|---|---|
| $CeO_2$/SACe-N-C | 0.384 | 0.842 | 0.94 V | This work |
| Ag-$CeO_2$-$Co_3O_4$/C | 0.484 | 0.80 | - | 13 |
| Ce SAS/HPNC | 1.02 | 0.86 | 1.04 | 14 |
| SACe-N/PC | 0.1 | 0.88 | - | 15 |
| $La_{0.7}Ce_{0.3}CoO_3$ | 1.0 | 0.75 | 0.87 | 16 |
| $Sm_2O_3$–Co/NEC300J | 0.146 | 0.811 | 0.924 | 17 |
| MnOOH@$CeO_2$ | 0.244 | 0.80 | 0.91 | 18 |
| $CeO_2$@NC-900 | 0.2 | 0.854 | 0.905 | 19 |
| Ce-$MnO_2$/C | 0.5 | 0.783 | 0.872 | 20 |

| | | | | |
|---|---|---|---|---|
| Co-$CeO_2$/N-CNR | 0.21 | 0.834 | - | 21 |
| $Co_3O_4$-$CeO_2$/KB | 0.1 | 0.83 | - | 22 |

**Table S6**. ECSA ($m^2 g^{-1}$) of prepared catalysts from 0.9163V to 1.0163V.

| | $CeO_2$/C | N-C | $CeO_2$/SACe-N-C |
|---|---|---|---|
| ECSA | 4.25 | 60 | 937.5 |

**Table S7**. Contents of different N species in $CeO_2$/SACe-N-C catalysts before and after charging and discharging batteries.

| | Pyridinic-N | Graphitic-N | Oxidized-N |
|---|---|---|---|
| $CeO_2$/SACe-N-C | 29 % | 61 % | 10 % |
| Spent $CeO_2$/SACe-N-C | 30 % | 61.7 % | 8.3 % |

**References**


1. Izumi; Momma, VESTA 3 for three-dimensional visualization of crystal, volumetric and morphology data. *Journal of applied crystallography* **2011**, *44* (6), 1272-1276.
2. Pan, J.; Shao, X.; Xu, X.; Zhong, J.; Ma, L. J. T. J. o. P. C. C., Organic Dye Molecule Sensitization Enhanced Photocatalytic Water-splitting Activity of $MoS_2$ from First-principles Calculations. *The Journal of Physical Chemistry C* **2020**, *124* (12), 6580-6587.
3. Zhang, W.; Zou, G.; Choi, J. H. J. A. O., Adsorption Behavior of the Hydroxyl Radical and Its Effects on Monolayer $MoS_2$. *ACS omega* **2020**, *5* (4), 1982-1986.
4. Li, J.; Zhang, S.; Wang, Y. P.; Duan, H. M.; Long, M. J. A. A. N. M., First Principles Study of Strain Modulation in $S_3P_2$/Black Phosphorene vdW Heterostructured Nanosheets for Flexible Electronics. *ACS Applied Nano Materials* **2020**, *3* (5), 4407-4417.
5. Lee, J.; Yoon, M. J. A. P. S., Strain engineered optoelectronic properties of transition metal dichalcogenides lateral heterostructures. *2D Materials* **2017**, *4* (2), 021016.
6. Ping, L.; Jin, Y. L. J. A. A. M.; Interfaces, GeC/GaN vdW Heterojunctions: A Promising Photocatalyst for Overall Water Splitting and Solar Energy Conversion. *ACS applied materials & interfaces* **2020**, *12* (12), 14289-14297.
7. Zhou, Z.; Zhang, Y.; Zhang, X.; Niu, X.; Wu, G.; Wang, J. J. J. o. M. C. A., Suppressing photoexcited electron–hole recombination in $MoSe_2$/$WSe_2$ lateral

heterostructures via interface-coupled state engineering: a time-domain ab initio study. *Journal of Materials Chemistry A* **2020**, *8* (39), 20621-20628.

8. Grimme, S. J. J. o. C. C., Semiempirical GGA-type density functional constructed with a long-range dispersion correction. *Journal of computational chemistry* 2006, *27* (15), 1787-1799.
9. Han, S. W.; Kwon, H.; Kim, S. K.; Ryu, S.; Yun, W. S.; Kim, D. H.; Hwang, J. H.; Kang, J. S.; Baik, J.; Shin, H. J. J. P. R. B., Band-gap transition induced by interlayer van der Waals interaction in $MoS_2$. *Physical Review B* **2011**, *84* (4), 045409.
10. C.; Ataca; H.; ahin; S.; Ciraci In *Stable,* Single-Layer $MX_2$ Transition-Metal Oxides and Dichalcogenides in a Honeycomb-Like Structure. *The Journal of Physical Chemistry C* **2012**, *116* (16), 8983-8999.
11. Nørskov J K, Rossmeisl J, Logadottir A, et al. Origin of the overpotential for oxygen reduction at a fuel-cell cathode. *The Journal of Physical Chemistry B* **2004**, *108* (46), 17886-17892.
12. Zhang T, Anderson A B. Oxygen reduction on platinum electrodes in base: Theoretical study. *Electrochimica Acta* **2007**, *53* (2), 982-989.
13. Li, T.; He, Z.; Liu, X.; Jiang, M.; Liao, Q.; Ding, R.; Liu, S.; Zhao, C.; Guo, W.; Zhang, S. J. S.; Interfaces, Interface interaction of Ag-$CeO_2$-$Co_3O_4$ facilitate ORR/OER activity for Zn-air battery. *Surfaces and Interfaces* **2022,** *33*, 102270.
14. Zhu, M.; Zhao, C.; Liu, X.; Wang, X.; Zhou, F.; Wang, J.; Hu, Y.; Zhao, Y.; Yao, T.; Yang, L.-M. J. A. C., Single atomic cerium sites with a high coordination

number for efficient oxygen reduction in proton-exchange membrane fuel cells. *ACS Catalysis* **2021,** *11* (7), 3923-3929.

15. Li, J.-C.; Qin, X.; Xiao, F.; Liang, C.; Xu, M.; Meng, Y.; Sarnello, E.; Fang, L.; Li, T.; Ding, S. J. N. l., Highly dispersive cerium atoms on carbon nanowires as oxygen reduction reaction electrocatalysts for Zn-air batteries. *Nano letters* **2021,** *21* (10), 4508-4515.
16. Sun, Y.-R.; Zhang, X.; Wang, L.-G.; Liu, Z.-K.; Kang, N.; Zhou, N.; You, W.-L.; Li, J.; Yu, X.-F. J. C. E. J., Lattice contraction tailoring in perovskite oxides towards improvement of oxygen electrode catalytic activity. *Chemical Engineering Journal* **2021,** *421*, 129698.
17. Li, D.; Sun, L.; Hu, L.; Zhu, J.; Shi, J.; Guo, D. J. J. o. P. S., Rare earth insitu-doped ZIF-67 derived N doped C encapsulated $Sm_2O_3$/Co nanoparticles as excellent oxygen reduction reaction catalyst for Al-air batteries. *Journal of Power Sources* **2021,** *482*, 229052.
18. Liu, D.; Tian, J.; Tang, Y.; Li, J.; Yi, S.; Huang, X.; Sun, D.; Wang, H. J. C. E. J., High-power double-face flow Al-air battery enabled by $CeO_2$ decorated MnOOH nanorods catalyst. *Chemical Engineering Journal* **2021,** *406*, 126772.
19. Kang, Y.; Wang, W.; Li, J.; Mi, Y.; Gong, H.; Lei, Z. J. J. o. C.; Science, I., 3D Rosa centifolia-like $CeO_2$ encapsulated with N-doped carbon as an enhanced electrocatalyst for Zn-air batteries. *Journal of Colloid and Interface Science* **2020,** *578*, 796-804.
20. Sun, S.; Xue, Y.; Wang, Q.; Huang, H.; Miao, H.; Liu, Z. J. E. A., Cerium ion

intercalated $MnO_2$ nanospheres with high catalytic activity toward oxygen reduction reaction for aluminum-air batteries. *Electrochimica Acta* **2018,** *263*, 544-554.

21. Sivanantham, A.; Ganesan, P.; Shanmugam, S. J. A. C. B. E., A synergistic effect of Co and $CeO_2$ in nitrogen-doped carbon nanostructure for the enhanced oxygen electrode activity and stability. *Applied Catalysis B: Environmental* **2018,** *237*, 1148-1159.
22. Liu, K.; Huang, X.; Wang, H.; Li, F.; Tang, Y.; Li, J.; Shao, M. J. A. A. M.; Interfaces, $Co_3O_4$-$CeO_2$/C as a highly active electrocatalyst for oxygen reduction reaction in Al–air batteries. *ACS Applied Materials & Interfaces* **2016,** *8* (50), 34422-34430.